

A Novel Shaped Ultrawideband Fractal Antenna for Medical Purposes

Hiwa Taha Sediq (✉ hiwa_eece@yahoo.com)



Department of Information Technology/ Erbil Polytechnic University <https://orcid.org/0000-0003-3888-2785>

Research Article

Keywords: Epsilon shape, Tumor Detection, Ultra-wideband antenna, Cancer, Power Loss Density, Specific Absorption Rate

Posted Date: January 19th, 2023

DOI: <https://doi.org/10.21203/rs.3.rs-1961953/v1>

License:   This work is licensed under a Creative Commons Attribution 4.0 International License.
[Read Full License](#)

A Novel Shaped Ultrawideband Fractal Antenna for Medical Purposes

Hiwa Taha Sediq^{1*}

“Department of Information Technology, Shaqlawa Technical College, Erbil Polytechnic University, Erbil,”Iraq¹

Abstract: An ultra-wideband (UWB) fractal antenna based on a new epsilon-shaped geometry is described in this paper for microwave applications in the medical field. The antenna geometry is designed by combining four epsilon shapes and three pairs of straight-line conductors. The new configuration has an impedance bandwidth ranging from 2.58 to 20.95GHz. The size of the designed antenna is 26 mm x 22 mm ($0.22\lambda_L \times 0.19\lambda_L$) with a wavelength of 116.3mm. For a novel design technique, a reconfigurable patch antenna is proposed for 3.6GHz (Wi-max), 5.4GHz (WLAN), 3.1-10.6 GHz (UWB), and all applications operating in the X band(8- 12 GHz) and Ku-band(12-18 GHz). ADS software is applied to configure and validate a comprehensive equivalent circuit model, and CST software is used to perform the full-wave analysis of the proposed antenna. A prototype of the suggested antenna is fabricated on a substrate of FR4 with a height of 1.6mm to confirm the entire wave investigation and the theoretical solution outcomes of the circuit. It is proved that the comparative outcomes of the measurement and simulation have a good agreement. The proposed antenna also provides a high realized gain magnitude of 7.21 dB at an operational frequency of 20.95GHz.

Keywords: Epsilon shape; Tumor Detection; Ultra-wideband antenna; Cancer; Power Loss Density; Specific Absorption Rate

1. Introduction

The progress of technology in the field of wireless communication relies heavily on the construction of antennas for mobile applications with improved radiation features. High efficiency, data rate, capacity, compactness, and other important aspects of the innovative propagation antenna. The Federal Communication Commission (FCC) assigned the frequency range communication of ultra-wideband devices to an operational range of 3.1-10.6GHz in 2002 [1-3]. Because of the continuing progress of ultra-wideband transmissions, a scientific revolution in modified antenna technologies has occurred to meet the important needs of these prototype schemes [4]. As a result, the investigators have sought to offer an ultra-wideband broadband radio technology to meet the needs of short and broadband operations. Since these UWB technologies have a high data rate and large bandwidth in microwave systems, they can send video, audio, and data files much quicker[5]. Multiple articles on various antenna designs have been published to demonstrate the profits of UWB applications in real world wireless communications. Furthermore, microwave antenna researchers all worldwide have attempted to construct ultra-wideband antennas utilizing a variety of bandwidth extension methods, such as feeding Coplanar Waveguide (CPW) [6], patch adjustment [7,8], and other feeding methods [9].

In the literature, several modified architectures for ultra-wideband applications have been presented [10–17]. The designers of [10] describe a bio-inspired UWB antenna with a pick gain of 3.63 dB for a broad communication of 3.4 to 8 GHz and a general dimension of 314×121 mm². Moreover, an asymmetric open slot antenna with an overall area of 29×20 mm² is printed on the Rogers 5880 substrate for UWB applications and works fine at an operational frequency of 3.1-10.8 GHz[11]. For the range communication frequency response, a high gain of 5.7 dB is attained by this antenna. Furthermore, the researchers of [12] provide a UWB antenna etched on the substrate of an RF-4 with a net size of 34×33 mm² and an obtained gain of 4.35dB

measured by the analyzer. However, for wideband operation, the measured gain of the structure is inconsistent. Another UWB antenna with a z-shaped and a 1.57 mm high substrate, a total area of 38 mm × 35 mm, and gain fluctuations of 1.6–6.4 dB has also been described [13]. However, near the frequencies of 8 GHz and 11 GHz, there is a divergence in impedance bandwidth for the UWB communication. The designers of [14] described an elliptical ring monopole antenna for UWB ranges that was manufactured on a 100×100 mm² ground plane. The planar antenna provides an average gain of 3.9dB in the whole ultra-wideband range. For UWB applications, a planar antenna with a pick gain of 4 dB [15] is proposed with dimensions of 26 mm × 25 mm. Another study on the UWB antenna, which operates in the 3.3GHz to 4.5 GHz frequency band, is published in [16]. Furthermore, a V-shaped patch antenna printed on a substrate of 4.4 is displayed in the article [17] that offers the greatest gain of 2.04dB for the entire broadband communications. Regarding earlier research, UWB antennas have massive constructions and some reach adequate impedance bandwidth, nevertheless, they have a small gain parameter.

This article is a novelty in that it introduces a new fractal epsilon-shaped geometry for medical UWB applications. Since the primary goal of this measuring system is to investigate the relationship between changes in backscattered signals from a throat model and breast phantom. This occurs due to changing dielectric properties inside the structure of both phantoms. The radiator structure is combined from four symmetrical epsilon shapes with three pairs of straight-line conductors printed on the dielectric substrate. The proposed antenna is fed via a microstrip method. Because of its dispersion and low radiation losses, this approach is a preferred option to feed antennas for wideband operation. The novel patch radiator achieves a wide bandwidth of 2.58-20.95 GHz with a fractional bandwidth of more than 157 percent by altering the ground plane and the fed line approaches. The using modern radiator and the ground plane structure provide better characteristic parameters of the planar antenna such as realized gain of 7.21 dB. The antenna design operates in the frequency communication of 18.4GHz with less reflection coefficient for the entire operating frequency. Table 1 displays the comparison of the low-profile designed antenna. As can be shown, the proposed UWB antenna has a wider bandwidth, a smaller electrical size and bandwidth ratio (BWR) than other ultra-wideband antennas listed in the table, and it even possesses a higher gain value for ultra-wideband communication systems

Table 1. Comparisons the suggested UWB antenna with other recorded recent antenna.

“[Ref.]	Size [mm ²]	Size [λ^2]	Frequency Range [GHz]	$F_h - F_L$ [GHz]	Substrate, h [mm], ϵ_r	BWR:1	Gain [dB]
[10]	314 × 121	3.56 × 1.37	3.4-8	4.6	FR-4, 1.6, 4.4	2.35	3.63
[11]	29 × 20	0.30 × 0.21	3.1-10.8	7.7	Rogers 5880, 1.57, 2.2	3.48	5.7
[12]	34 × 33	0.16 × 0.15	1.4-11.3	9.9	FR-4, 1.6, 4.4	8.07	4.35
[13]	38 × 35	0.35 × 0.33	2.8-22.7	19.9	Rogers 5880, 1.57, 2.2	8.11	6.4
[14]	100 × 100	1.03 × 1.03	3.1-12	8.9	-	3.87	4.8
[15]	26 × 25	0.28 × 0.27	3.2-12	8.8	FR-4, 1.6, 4.3	3.75	4
[16]	25.75 × 25.75	0.28 × 0.28	3.3-4.5	1.2	RO4350B, 0.254, 3.66	1.36	-
[17]	21 × 15	0.26 × 0.19	3.78-7.08	3.3	FR-4, 1.6, 4.4	1.87	2.04
Pro.	26 × 22	0.22 × 0.19	2.58- 20.95	18.4	FR-4, 1.6, 4.4	8.12	7.21”

2. Antenna Design Sketch

In this article, the proposed antenna is made up of three epsilon geometric shapes joined by the three pairs of the straight line. The microstrip conductor line of the proposed monopole ultra-wideband antenna is attached to the patch radiator. Some modification is made in the design of the unit cell antenna as modifying the width and shifting the position of the E-shaped stub

inserted into the patch in order to provide a suitable broad bandwidth for the design. The dimensional layout of the innovative unit cell antenna is given in detail in Figure 1. The selected dielectric material in this design for the planned antenna is the FR-4 dielectric substrate which has a relative permittivity (ϵ_r) of 4.4, a loss factor (δ) of 0.02, and a height (h) of 1.6 mm. The primary parameters of the proposed antenna are analyzed using the CST microwave simulation tool, and the structure is fed by 50 ohms via a copper conductive strip. The lower frequency (F_L) of the structural antenna is computed using a standard equation (1) [18]. The total area (A) of the patch antenna design is found by computing the area of all half-ring shapes and the rectangular geometries. Moreover, a standard equation (2) is used to find the constant value of $k = \sqrt[4]{\epsilon_{eff}}$ [19]. A low operating frequency of 2.62GHz is provided for the prototype antenna as a result of using the equations. The theoretical value of F_L is calculated and this value computed is quite close to those obtained by the tested analyzer. The unit cell antenna has a total volume of $(26 \times 22 \times 1.6) \text{ mm}^3$, and the ideal values of the innovative antenna's various dimensions are listed in Table 2.

$$F_L = \frac{c}{\lambda} = \frac{c}{[2 \times 2 \times \frac{A}{r}] \times k} \text{ GHz} \quad (1)$$

$$\epsilon_{eff} = \frac{\epsilon_r + 1}{2} + \frac{\epsilon_r - 1}{2} [1 + 12 \frac{h}{wf}]^{-\frac{1}{2}} \quad (2)$$

$$A = 190.88 \text{ mm}^2, \quad k = \sqrt[4]{\epsilon_{eff}} = 1.35$$

When the above results are applied to equation(1), the cutoff-frequency is found as:

$$F_L = \frac{3E + 11}{[2 \times 2 \times \frac{190.88}{9}] \times 1.35} = 2.62 \text{ GHz}$$

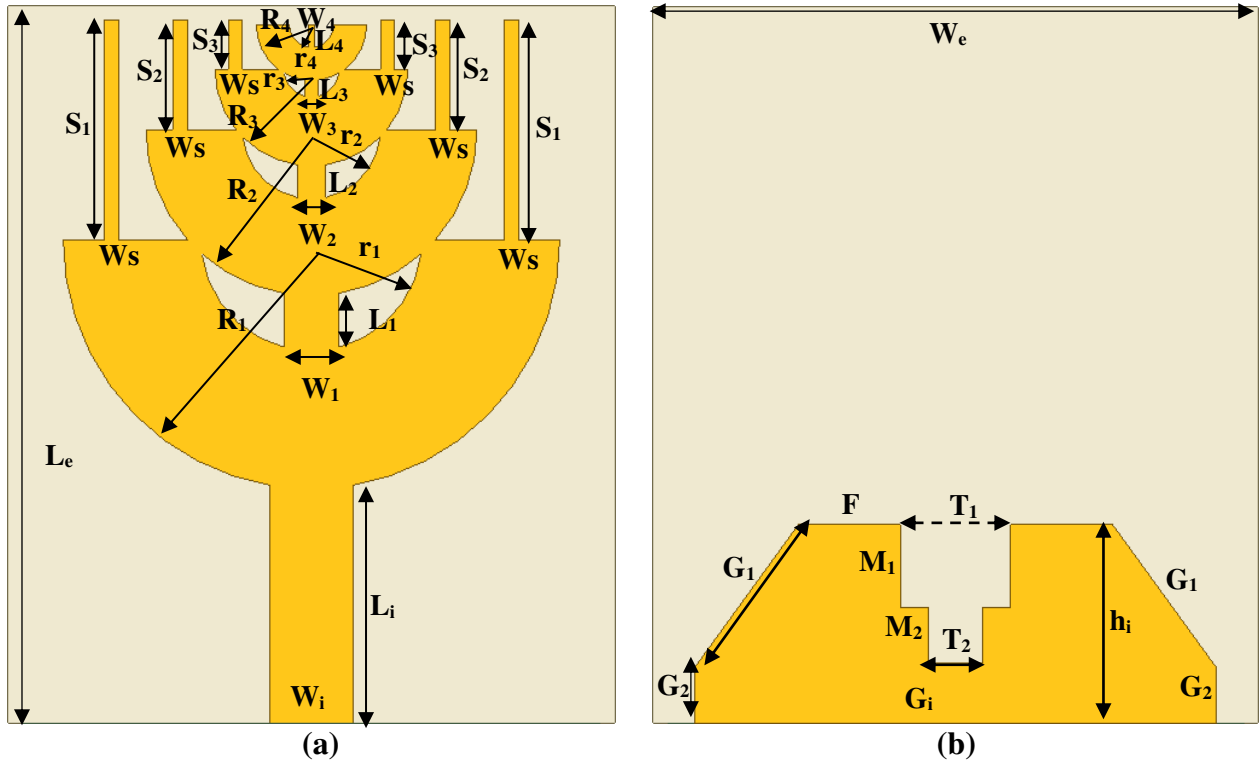


Fig.1. Sketch of single monopole UWB antenna

Table 2. The novel structure's parametric dimensions.

Parameters	Le	We	W ₁	W ₂	W ₃	W ₄	R ₁	R ₂	R ₃	R ₄	r ₁	r ₂	r ₃	r ₄	G ₁	G ₂
Dim. (mm)	26	22	2	1	0.5	0.2	9	6	3.5	2	4	2.5	1	0.8	6.4	2
Parameters	L _i	W _i	h _i	G _i	L ₁	L ₂	L ₃	L ₄	S ₁	S ₂	S ₃	W _s	T ₁	T ₂	M ₁	M ₂
Dim. (mm)	8.5	3	7.2	19	2	1.2	0.6	0.8	8	4	1.8	0.5	4	2	3	2

3. Procedure for Antenna Evolution

The proposed factual epsilon shape of the patch radiation is the result of several distinct stages in the geometrical radiation and the ground plane conductor printed on the dielectric substrate is given in Figure 2a. In order to obtain suitable properties of the Ultra-wideband antenna, a typical epsilon-shaped patch is linked to a strip fed-line in the first iteration. The antenna operates at two various resonance frequencies with a notched band from 10.5 to 10.9 GHz, however, the impedance bandwidth of the ultra-wideband antenna is insufficient during the entire frequency band. This is due to the quick modification in impedance bandwidth at the connection between the feeder and the radiator. Hence, the second epsilon shape iteration is inserted into the patch radiator to increase the bandwidth characteristic of the planar antenna in stage II. Due to this, the reflection coefficient (S_{11}) level in the notched band lowers to less than -15 dB. Furthermore, The operating communication of the lower frequency has been upgraded from 3.2 to 2.97 GHz, and the antenna frequency range is increased from 2.97 GHz to 20.2GHz.

The form of the antenna II is adjusted in the third stage by attaching another epsilon-shaped iteration to the antenna at the upper side of the copper patch. The reflection coefficient results in dB have been enhanced as a consequence of this adjustment and the minimum frequency operation of the monopole antenna is decreased from 2.97 to 2.86GHz. The condition of the operating range for the UWB applications is also obtained shown in the third iteration of Figure 2b. Another E-shaped geometry is inserted in the antenna IV stage into the monopole structure, in order to increase the frequency range of the monopole ultra-wideband antenna. This step improves the novel antenna's low-frequency responsiveness from 2.86 to 2.72GHz, and the antenna can operate in the 2.72-20.82 GHz frequency band. The operating range of the planar antenna is still extended from 2.72-20.82 GHz to 2.58 - 20.95 GHz using three pairs of straight-line coppers in the upper side of the epsilon shapes in the fifth antenna. As stated in Figure 2b, the impedance characteristic of the final geometrical configuration (Antenn. IV) reduces the S_{11} results over the whole working range.

The rectangular-shaped lines on the top patch structure of the planar antenna in the fifth design stage are also a cause to provide a good result for the proposed ultra-wideband antenna. Furthermore, this step is a purpose to reduce the capacitance impacts. Because when the overall capacitance effects drop, the antenna coupling value falls. Therefore, due to this reduction value, the capacitive impact is diminished and the response frequency range is extended as shown in Figure 2b. As a result of the UWB planar antenna's radiation and ground plane modifications, superior impedance matching is achieved over the impedance bandwidth range of roughly 2.5 GHz to larger than 21 GHz. Finally, the proposed UWB antenna can be used in wireless communication systems for various system communications in the S, C, X, Ku, and K frequency bands.

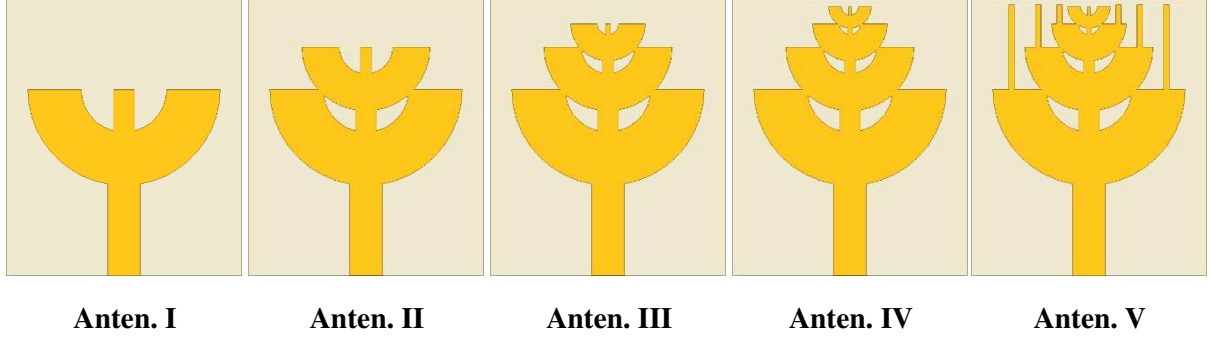


Fig.2. (a) The fractal epsilon-shaped ultra-wideband antenna's deriving stages.

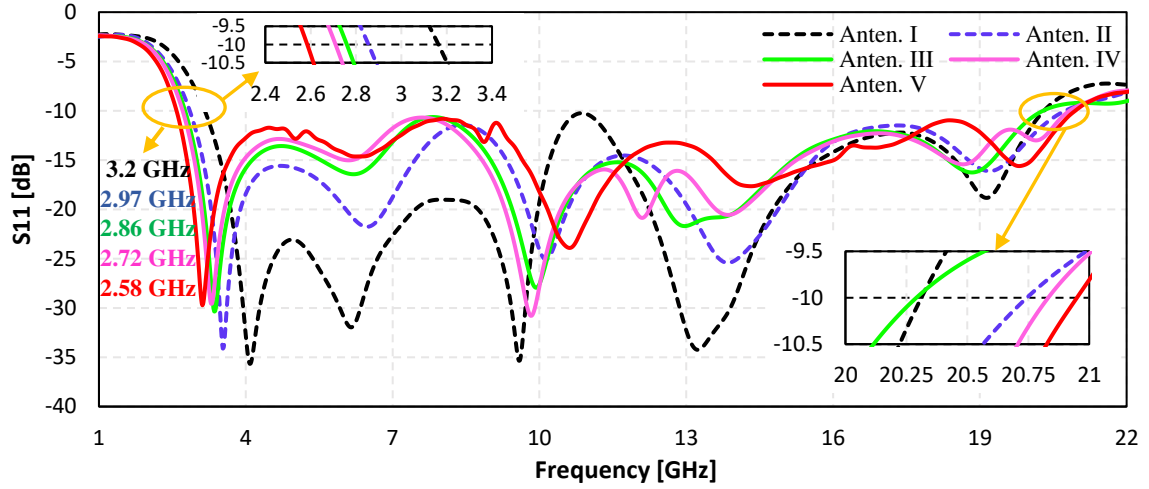


Fig.2. (b) Simulated S11 evaluation for various antenna levels.

4. UWB Antenna Equivalent Circuit

For a narrowband antenna, the LC resonant circuit is a decent approximation. Multiple LC resonators are cascaded in broadband antennas, and their resonant frequencies constantly overlap to create the whole wideband resonances of the UWB antenna. The Advanced Design System (ADS) software is used to draw the equivalent circuit of the ultra-wideband antenna, and its lumped element of the circuit is shown in Figure4a. The simulation results of the analogous circuit are compared to the ideal simulation as indicated in Figure4b. For computing LC elements, the imaginary and real impedances at operational frequencies are taken from the outcomes of the CST simulator [18]. Equation (3-4) is used to provide the L_0 and C_0 components for the transmission line of the proposed antenna in the equivalent circuit diagram [20]. The equations (5-6) are used to calculate the inductance and capacitance for the lumped circuit elements. The antenna equivalent circuit is drawn utilizing ADS software after combining component values and tuning them. The figure shows that the attained results of the CST and ADS software are in good agreement for the overall resonant frequencies and the values of the imaginary and real impedance around 50 ohms and 0 ohms respectively. The conclusive outcomes of the component circuit are achieved for the circuit as follows: $L_0=0.202$ nH, $C_0=0.13$ pF, $R_1=58.43 \Omega$, $L_1=1.696$ nH, $C_1=2.04$ pF, $R_2=62.67 \Omega$, $L_2=0.819$ nH, $C_2=0.97$ pF, $R_3=46.94 \Omega$, $L_3=0.156$ nH, $C_3=1.45$ pF, $R_4=61.09 \Omega$, $L_4=0.141$ nH, $C_4=0.73$ pF, $R_5=69.1 \Omega$, $L_5=0.089$ nH, $C_5=0.63$ pF.

$$L_0 = 100h \left(4 \sqrt{\frac{W_f}{h}} - 4.21 \right) \quad (3) \quad C_0 = W_f \left[(9.5\epsilon_r + 1.25) \frac{W_f}{h} + 5.2\epsilon_r + 7 \right] \quad (4)$$

$$L = \frac{\text{img}(Z_{11})}{2\pi f} \quad (5)$$

$$C = [(2\pi f)^2 L]^{-1} \quad (6)$$

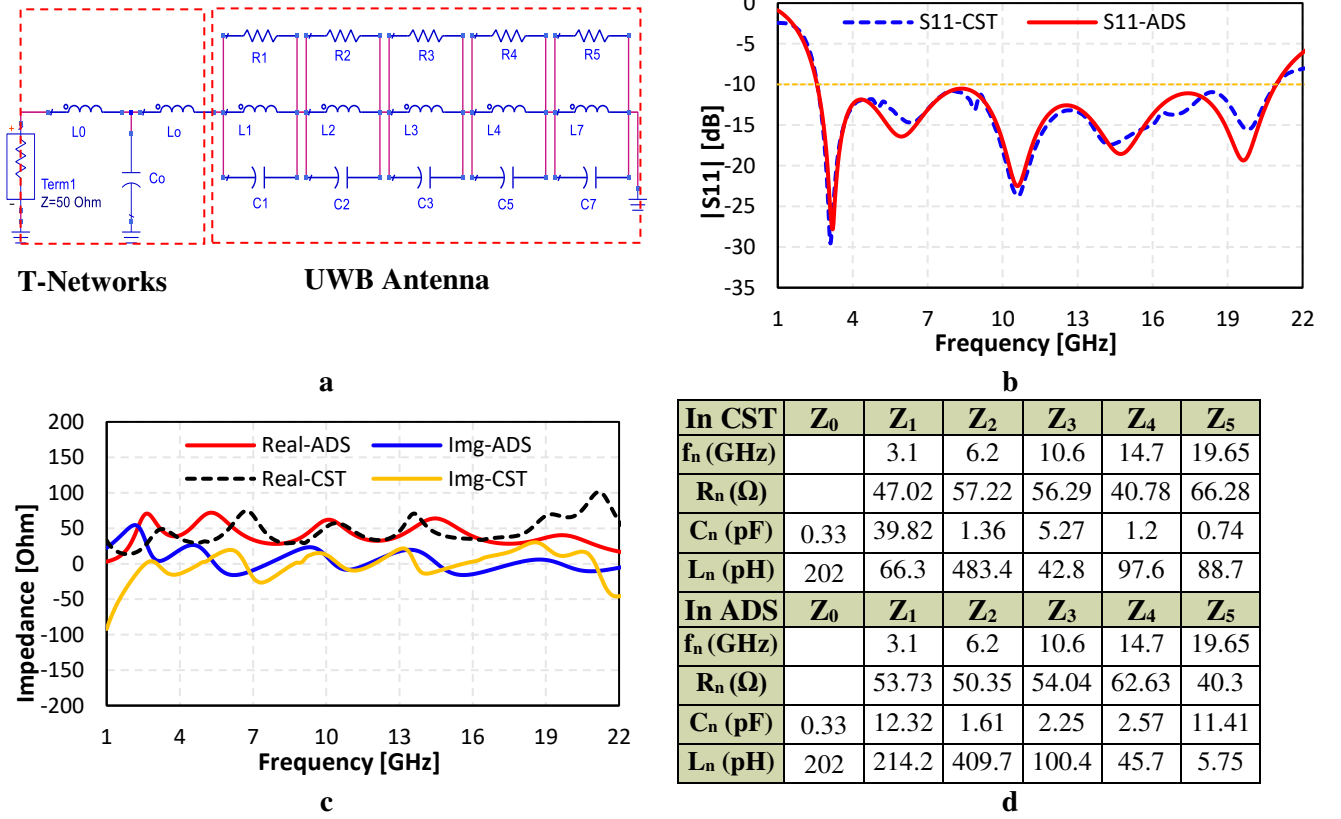


Fig. 3. (a) The equivalent circuit of antenna, ADS and CST outcomes is compared in (b), (c) and (d).

5. Discussion on the Results

This part discusses the experimental and simulation outcomes to investigate the property of the proposed design. The experimental photo in the front and back views linked to the SMA connector is exposed in Figure 4 for the fabricated antenna. The main parameters of the antenna prototype are measured using a Rhode & Schwarz ZVA 24GHz electronic instrument known as a Vector Network Analyzer (VNA). The fabricated UWB antenna operates perfectly with the 2.72 –19.97 GHz frequency spectrum. To study the model outcomes, the simulation results of the CST and HFSS microwave simulators are compared to the experimental data. The compared simulation and measurement S11 outcomes of the novel UWB monopole structure are shown in Figure 5. The measurement S11 result nearly matches the simulated S11 outcome in the entire operational frequency as seen in this figure. However, the result of the full operating frequency shows a minor deviation. This difference could be related to the use of PNA cables, manufacturing tolerances, and the SMA connector's stretched grounding effects, which are not present in the simulation component. Furthermore, this substrate is used as an ideal material condition for the simulated case, but this may not be attainable in practical analysis, thus the tolerance of the substrate structure also affects the results. The CST simulator activates at frequencies operating from 2.58GHz to 20.95GHz, whereas the HFSS simulated software works at frequencies ranging from 2.77GHz to 20.86GHz. As shown in Figure 5, the measured S11 findings begin at an operational frequency of 2.72 GHz and go up to 19.97 GHz in the measurement part.

The proposed antenna has a reasonably simulated bandwidth ratio of 8.12:1 and a fractional frequency band of 157 percent in the frequency range 2.58-20.95 GHz. The fabricated antenna

gives an operational frequency of 2.72 to 19.97GHz in the measuring section, with a bandwidth ratio of 7.34:1 and a fractional bandwidth of roughly 152 percent. As a result, for future portable applications, the low profile UWB antenna confirms a high impedance bandwidths. The innovative construction of the antenna also represents two significant advantages: high bandwidth and compactness.

The gain parameter is another significant characteristic study of the examined UWB design. This is investigated to better understand the efficiency of the designed antenna. Figure 6 shows a comparison of the measured and simulated gain fluctuation of the proposed antenna. The gain value increases with respect to increasing the range of the operational frequencies, as shown in the figure. As a result of increasing wavelength, the effective aperture of the proposed antenna grows. Because of increasing current density at the sharp edges of the monopole antenna, the gain curve varies across the whole frequency range. The simulated outcomes of the parametric realized gain change between 1.61 dB and 6.73 dB, and at the frequency of 20.95GHz, a maximum simulated gain of 7.21 dB is obtained. In the measurement part, the maximum gain of the fabricated structure is 7.04 dB provided when operating at 19.61 GHz, and the experimental results of the obtained gain vary between 1.06 and 6.76 dB. The radiation efficiency of the proposed antenna simulation results fluctuates with frequency from the selected operational frequency. As can be realized in Figure 6, the average attained efficiency at the operating frequency of the proposed antenna is above 90% and 85% in the simulation and measurement results, respectively and the values of this efficiency improve with increasing frequency.



Fig. 4. Fabricated picture of the UWB antenna in the front and back views.

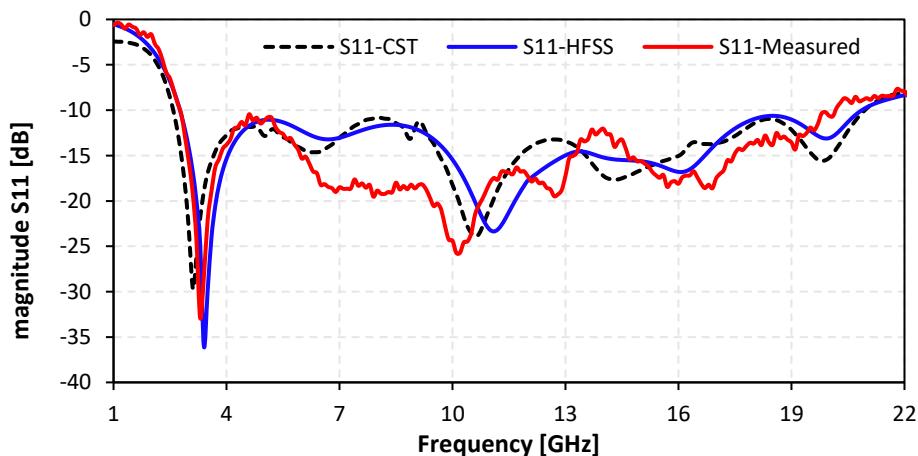


Fig. 5. Comparison of Simulated and Measured S_{11} outcomes.

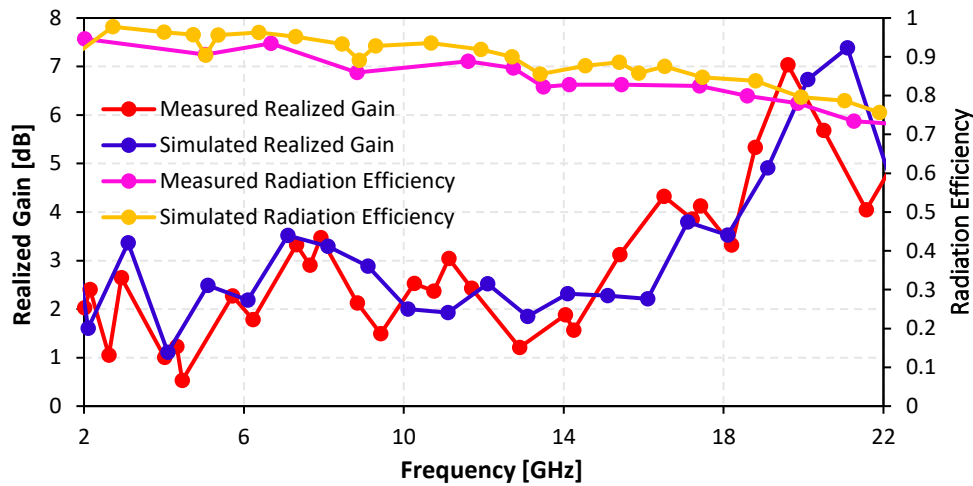


Fig. 6. Gain fluctuation curve and radiation efficiency with frequency.

In order to describe the parametric radiation patterns at the different frequencies of 3.5, 7 and 10.5GHz, the H planes ($\phi=0^\circ$) and E ($\phi=90^\circ$) are investigated. The radiation patterns of the proposed antenna are measured in an automatic anechoic chamber and the pattern is recorded at each rotation step at a distance of 2 meters between the design structure and the reference horn antenna. At frequencies of 3.5 and 7 GHz, the measured and simulated H-field patterns are closely omnidirectional in shape, as shown in Figure 7. Furthermore, this pattern is nearly a cardioid radiation pattern for H-plane simulation and measurement at 10.5GHz frequency. At frequencies of 3.5GHz, the E-field radiation pattern is nearly bidirectional and this pattern exhibits a kidney-shaped radiation pattern at the frequency of 7 GHz for simulation and measurement test, whereas the radiation pattern of UWB antenna at a high frequency of 10.5 GHz is an omi-directional pattern. At the H and E planes, the radiation pattern becomes distorted omnidirectional and bidirectional while increasing the frequency. The high frequency mode activation at higher frequencies causes this distortion. Furthermore, the current density is unevenly distributed throughout the radiator due to inducing higher order modes at high operating frequencies. As a result of the radiation mode, the magnitude percentage of electromagnetic interference increases. Researchers employ a range of strategies to reduce undesirable radiation modes, including defective ground structures, periodic structures, splitting resonators, parasitic elements, and so on. The measurement and simulation outcomes are acceptable with slight deviations in both radiations of the H and E planes. It is due of the environmental effects of the surrounding device, radiation effects, and electromagnetic interference from the antenna array's elements.

For three different frequencies of 3.5GHz, 7GHz, and 10.5GHz, Figure 8 shows the simulation results of a 3-dimensional plot of the proposed ultra-wideband antenna's polar gains. The polar patterns are omnidirectional at the low and mid resonances for pick gains of 2.49dB and 3.6dB, respectively, as indicated in the figure. The shaped pattern gives cardioid features with tiny back lobes at the operational frequency of 10.5 GHz. As a result, the planar antenna's maximum simulated gain of roughly 2.92 dB is estimated at the upper resonance frequency of 10.5GHz, as shown in Figure 8c.

At particular resonant frequency points, the surface current distribution is considered extra to study the resonant behaviours of the designed ultra-wideband antenna, as displayed in Figure 9. At the new patch edges, around the ground plane, stub conductor, and line feeder, the largest current density is observed. This distribution pattern at low resonances of 3.5GHz demonstrates the first harmonic mode. the current distribution at the middle and high resonances of 7GHz and 10.5GHz looks to be a higher harmonic mode. So as to attain a large working

communication range, it is critical to overlap neighbouring modes on one another while scheming a UWB antenna. The surface current of the planar antenna in the patch radiator and ground plane keeps the harmonic order flux to achieve the UWB system. The structure expands the surface current length by using the geometrical epsilon-shaped radiator and the inverted L-shaped stub joined to the ground part. As a result, the wideband operational properties of the innovative ultra-wideband antenna are provided by this method.

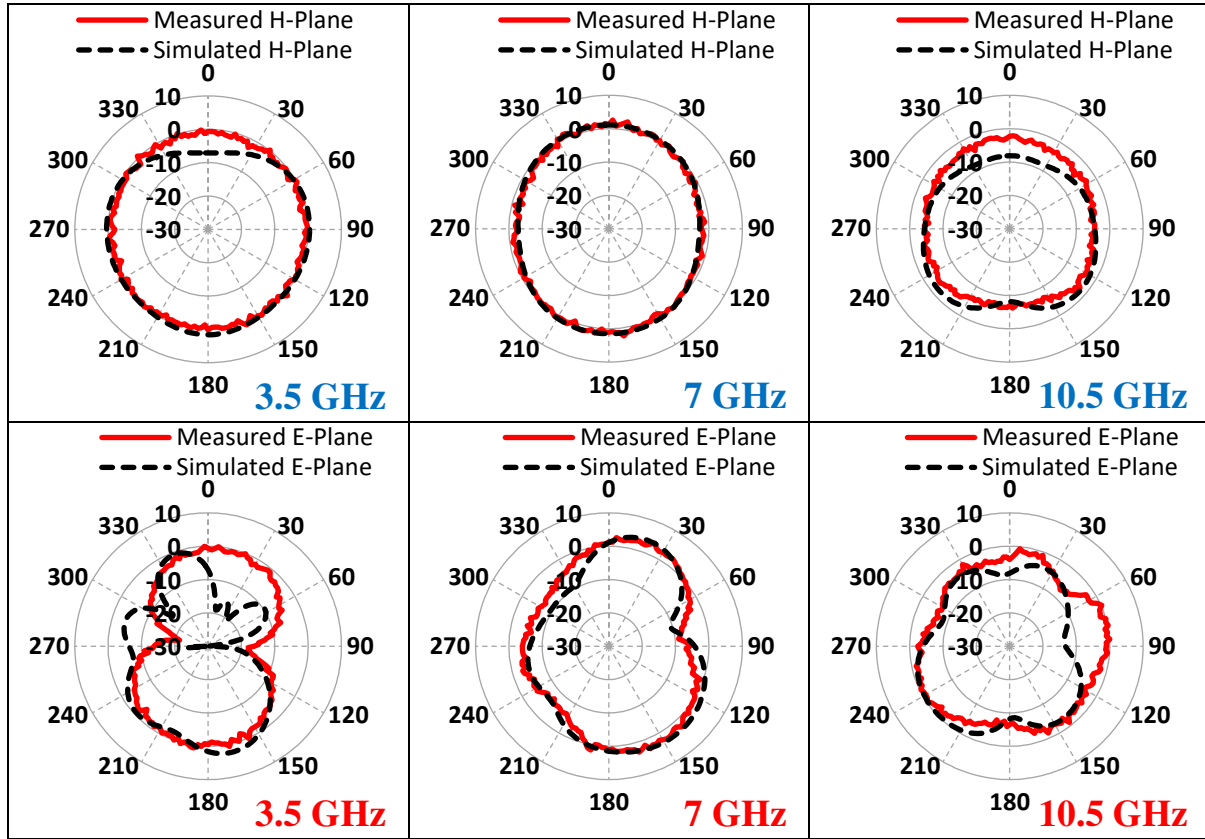


Fig. 7. Measured and simulated far-field radiation pattern for E and H plane at frequency of 3.5GHz, 7GHz, and 10.5GHz.

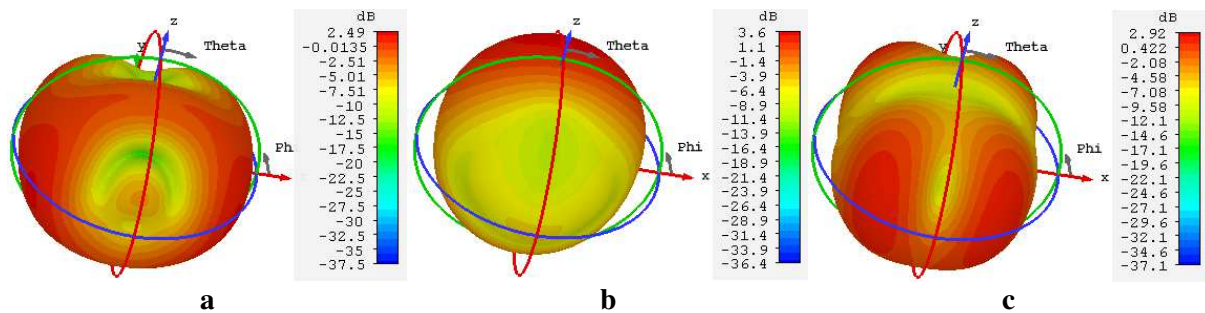


Fig. 8. Gain polar plot at (a) 3.5GHz, (b) 7GHz, (c) 10.5GHz frequency.

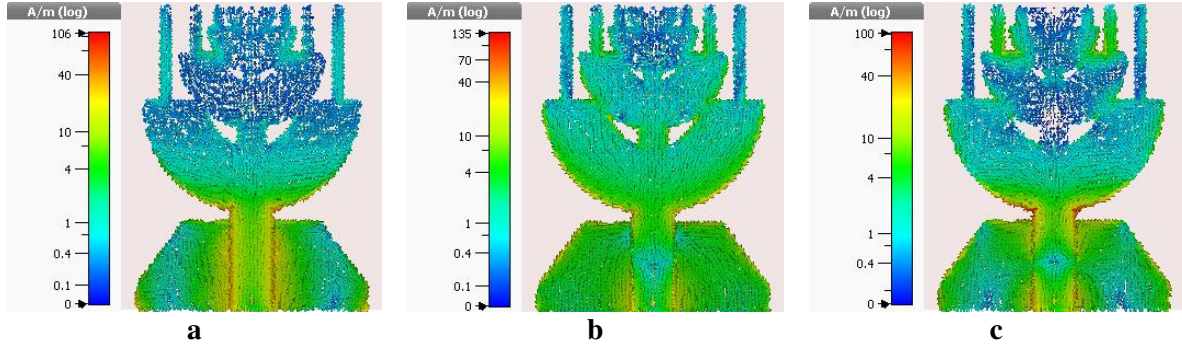


Fig. 9. Surface current picture at the different resonance (a) 3.5GHz, (b) 7GHz, (c) 10.5GHz.

6. Analyzing Time Domain

Understanding the pulse-forming features of UWB antennas requires time-domain study. The examined signal has a timing difference of a few hundred picoseconds. For the UWB antenna, the obtained pulse shape should be the same as the transmission pulses in the ideal scenario. In practice, however, incoming signals have a tendency to skew in form, resulting in a lengthy tail known as the "ringing effect." The antenna should be wisely evaluated for this reason to avoid distortion. A pair of low-profile UWB antennas with the same dimensional size are designed and positioned at a selected range of 30 cm in this research. Two alternative arguments are reviewed face to face (FtF) and side by side (SbS) for a further evaluation of the wave signals, as exposed in Figure 10. In both circumstances, Gaussian pulses are employed to examine the receiving and transmitting pulse shapes, as revealed in Figure 11a. The fidelity factor (FF) is an important time-domain metric utilized to show the parity between output and input pulses. The correlation between received and sent waveforms is likewise controlled by this parameter and Equation (7) can be typically used to calculate the antenna fidelity factor. The value of this factor is usually set between 0 and 1 after normalization. When the fidelity value reaches the 0 value, the coming signal will be entirely unlike the wave shape of the output signal because of system attenuation. For both scenarios, the fidelity coefficients are plotted against time variation in Figure 11b. As illustrated in the figure that the FFs acquired between the reception and transmission of the wave pattern in SbS and FtF processes are 89% and 81%, individually. The similarity coefficient between the signal outlines is higher in the side by side scenario than in the face to face scenario. This is because of a distortion in the wave pattern of the face to face case. As a result, a high fidelity parameter value decreases the distortion and ensures an acceptable match between the received and transmitted signals.

$$Fidelity\ Factor = \left[\frac{\int_{-\infty}^{\infty} T(t)R(t + \tau)dt}{\int_{-\infty}^{\infty} |T(t)|^2 dt \int_{-\infty}^{\infty} |R(t)|^2 dt} \right] \quad (7)$$

where the received signal is $R(t)$, and the sending pulse waveform is $T(t)$ for the two matching geometries.

The time delay of receiving and transmitting waveforms is analyzed using the group delay (GD) parameter, which is the next essential time domain parameter. The derivative of the negative sign of the phase variation with frequency is used to demonstrate this parameter numerically. The signal is distorted in both amplitude and phase during transmission when it passes through the device. As the signals are entered into the apparatus, the waves include several frequency components. Therefore, the signal phase distortion of the input wave patterns at specific frequencies is expressed by this delay. This parameter also specifies the linearity of the phase response in the far-field area. For measurement purposes, dual antennas are placed in the range of 300 mm apart. The measured and simulated outcomes of the group delay are

explored in face to face and side by side scenarios for the proposed UWB antenna. In both situations, the simulated delay parameter curve changes between 0.5 and 1.5 nanoseconds, but the experimental group delay outcomes vary between 0.7 and 1.5 nanoseconds, as illustrated in Figure 12. Over the total frequency range, the distortion rate of the FtF output wave pulse is higher than that of the SbS setup. However, there is a small variance between the measurement and simulation results due to noise in the measurement system, which is evidenced by the linear phase reaction across the desired operation. This analysis demonstrates that appropriate time domain parameter outcomes can be obtained at the general operational frequency, which in both cases is between around 1 and less than 2 ns. The modest value of the group delay is very important to obtain a good UWB system and the using equation (8) calculates this parameter as.

$$\tau_g(\omega) = \frac{d\phi(\omega)}{d\omega} = \frac{d\phi(\omega)}{2\pi df} \quad (8)$$

where ϕ is the transmitted pulse's phase variation and ω is the angular frequency.

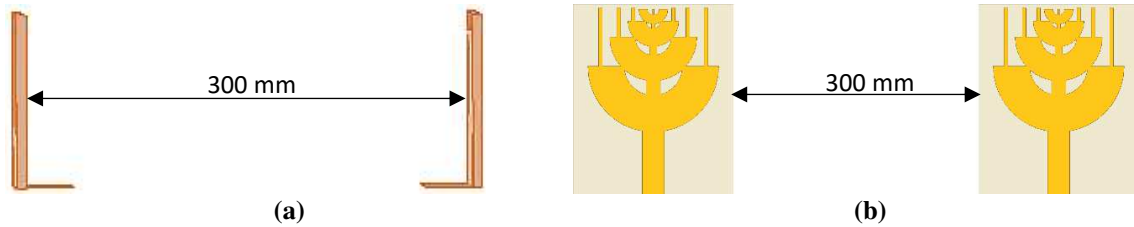


Fig. 10. Analyzing time-domain in (a) FtF and (b) SbS arguments.

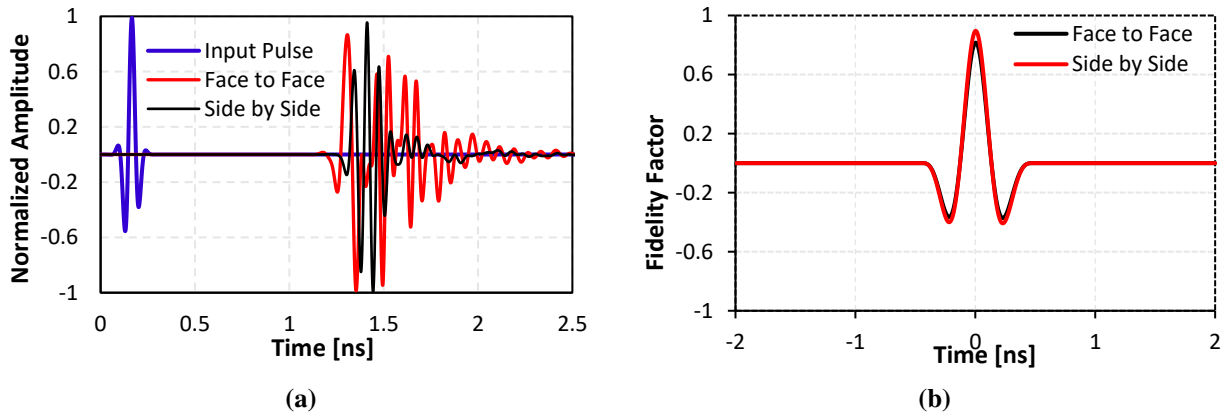


Fig. 11. (a) Normalized input and output signal pulses simulation in the time domain; (b) fidelity coefficients against time.

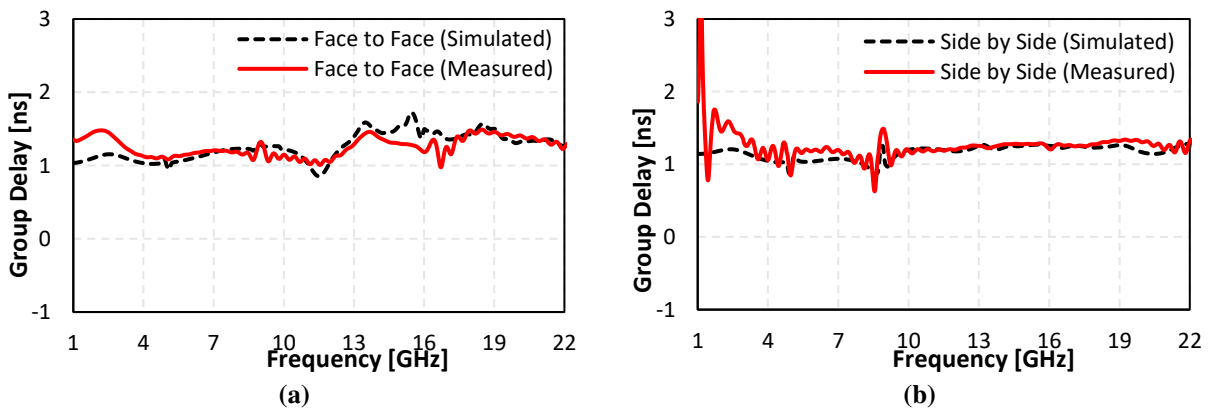


Fig. 12. Comparing GD vs. frequency in (a) FtF and (b) SbS situations.

7. Study on Cancer Detection

Cancer is one of the most complex diseases, and if it is not detected early enough, it can lead to death. According to statistics, 13.2 million cancer deaths are projected in 2030 [21]. The importance of early cancer identification for effective therapy cannot be overstated. Cancer can be detected in a variety of methods, depending on the stage at which the malignant tumors are discovered. In the early phases of tumor detection, basic procedures such as x-rays, ultrasound, computed tomography (CT) scan, magnetic resonance imaging (MRI) scan, and biopsy are used. In cancer detection, microwave tomography and microwave imaging approaches [22] have been examined. The electric field distribution is reconstructed in microwave tomography by solving the inverse non-linear function problem. Ultra-wideband pulses are broadcast from an antenna array that surrounds the human body using radar-based microwave imaging techniques, which is a costly approach.

Microwave imaging emerged from prior detection techniques that used electromagnetic radiation in the microwave domain to detect hidden objects (300 MHz - 300 GHz). The tumorous cells' electrical characteristics differ from those of the surrounding healthy tissues, which allows for detection [23]. Recent advances in technology, particularly the usage of ultra-wideband (UWB) devices, have improved detection resolution. A breast tumor was detected using an ultra-wideband antenna in paper [24, 25] by evaluating fluctuations in current density and specific absorption rate. The antenna's fluctuations in return loss were further analyzed by modeling the antenna on a breast phantom with and without a tumor [26]. The quantity of energy dispersed from the antenna was measured to detect tumors in paper [27]. When the antenna is pointed at cancer, more energy is dispersed than when the antenna is pointed away from the cancerous cells. This paper proposes a compact metamaterial-based planar patch antenna for effective breast and throat tumor detection. The computer simulation technology microwave studio (CST) is used to design and simulate the proposed antenna based on the finite integration technique. The suggested antenna is simulated separately on a breast phantom and throat with and without tumor, and variations in S-parameters, specific absorption rate, and power pattern in the presence of tumor demonstrate the effective performance of the antenna.

7.1. Design breast and throat

The main proposed of breast phantom measurement is to compare changes in the backscattering signal with the existence of high dielectric objects, such as a tumor. In this paper, an automated microwave imaging system is developed as Figure 13a depicts the imaging system's block diagram. A single PC controls all of the devices and electromechanical circuits. The transceiver is comprised of antennas, and a vector network analyzer (VNA) is used to collect the scattering signals. A different mechanical technique is employed for gathering data across the breast phantom from the measuring setup. The mechanical rotation platform is capable of rotating in polar coordinates ranging from 0 to 2π . The spinning platform is controlled by an Arduino Uno circuit through a stepper motor. A total of 360° rotations are conducted, with measurements taken at 120 equivalent locations separated by 30 degrees. Due to the continuing safety approval, no human bodies or patients are used in this case. the phantom is rotated to gather data throughout the phantom in order to pinpoint the tumor's site in the laboratory tests. The rotating platform will be configured in the resulting system to function as a medical imaging bra that rotates clockwise. For evaluating the system, a homogenous breast phantom containing a single tumor is used with a higher dielectric constant. Figure 13b shows a commercially accessible off-the-shelf breast phantom created in Japan that meets the required conditions. The phantom size is roughly $12 \times 6 \text{ cm}^2$, with the dielectric constant of a human breast and an 8 mm diameter target tumor within. The phantom is made up of four layers: the skin layer, the fat layer, the tumor, and the normal air layer. The dielectric constant and

conductivity of the skin layer are 38 and 1.49 S/m respectively with a thickness of 2 mm. The maximal width of the breast tissue layer or fat layer is 7.6 cm, with a dielectric constant = 5.14 and conductivity of 0.141 S/m. The conductivity of the tumor is 3.1 S/m with a dielectric constant of 67 [28]. Both antennas are placed parallel at 14 cm apart in the face to face case, and the distance of each antenna from the breast skin layer is 12 mm. The proposed antennas are connected to the VNA and the breast phantom is put on the rotation platform that is positioned near the analyzer (ZVA 24 GHz). The VNA is linked to a PC through a GPIB connection, and data is transferred to the PC using this configuration as shown in Figure 13c. For the throat study, A sample of the neck segment is considered with the throat size of $(54 \times 36 \times 42 \text{ mm}^3)$ for detection of throat tumor and this includes five layers such as the skin layer, the fat layer, the thyroid gland, the tumor, and the trachea as shown in Figure 14b. The thickness of the skin layer is 2.5 mm with a dielectric constant of 38 and the conductivity of 1.49 S/m. The dielectric constant and conductivity of the fat layer are 5.14 and 0.141 S/m respectively with a thickness of 2 mm. The conductivity of the tumor is 3.1 S/m with a dielectric constant of 67 [28]. Each tracheal ring is an average of 4 mm in height and there are approximately two cartilage rings per centimeter of the trachea. The typical exterior diameter of the trachea is 2.6 cm and the trachea's wall is around 3 mm thick on average [29] as shown in Figure 14b. The two proposed antennas are placed on the right and left sides of the throat to record the tumor effect of the dielectric constant on the transmission and reflection signals using the VNA. the distance between the planar antennas is 88 mm and each of them is apart from the skin layer in a range of 20 mm. The vector network analyzer is connected to a computer through a GPIB connection to collect the data of the signals as depicted in Figure 14c. Lastly, the effects of normal and unhealthy breast tissue can be studied and investigated using the forward and backscattering signal processes.

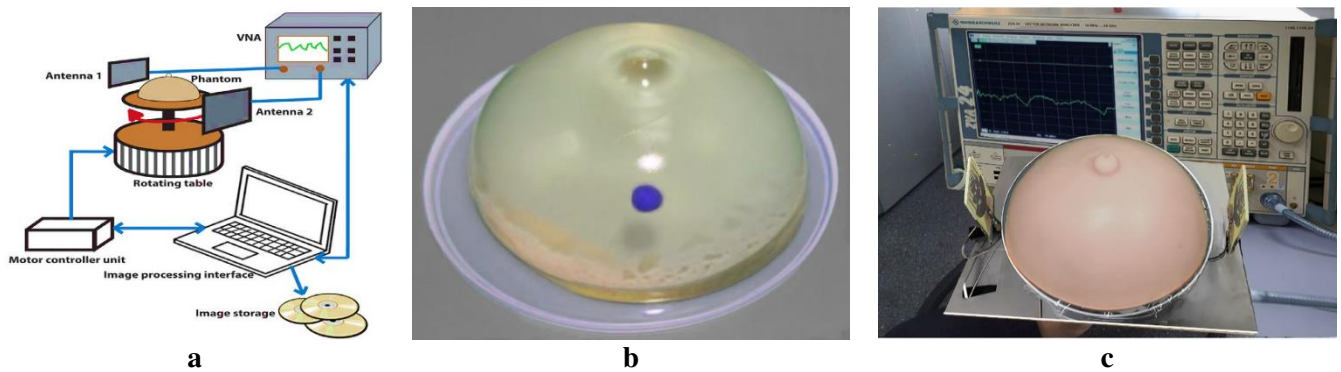


Fig. 13. Plot of (a) Block diagram of the imaging system, (b) Breast phantom with a single tumor, and (c) Measurement setup for the phantom breast between the antennas.

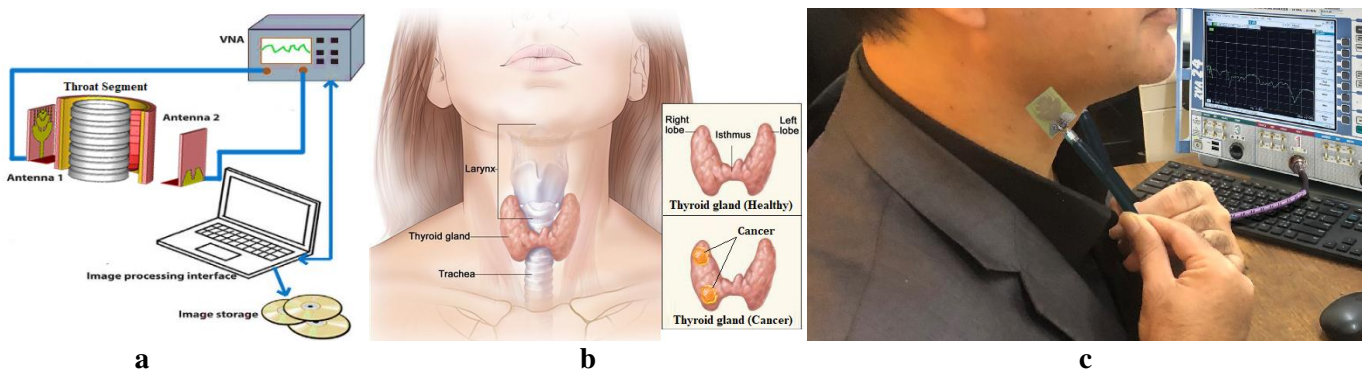


Fig. 14. Plot of (a) Block diagram of the imaging system, (b) Throat phantom with tumors, and (c) Measurement setup for the phantom throat between the antennas.

7.2.Experiment and Result Discussion

The CST microwave studio is used to create an experimental setting for detecting tumors in a human breast and throat model in the simulation part. The physical foundations of UWB-based cancer detection work by determining the difference between normal and malignant tissue based on the dielectric characteristics of the normal and malignant tissues. The difference between the dielectric characteristics of the skin and the internal tissues results in scattering signals, undesired reflections, and multipath effects [25]. The impulse response of the antennas employed in this proposed experiment is used to examine these effects and identify the cancerous tissue. Both the breast model and throat sample are placed between the two parallel UWB antennas as shown in Figure 15 that they act as a transmitter (antenna 1) and receiver (antenna 2) metamaterial antennas. Since the primary goal of this measuring system is to investigate the relationship between changes in backscattered signals from a throat model and breast phantom. This occurs due to changing dielectric properties inside the structure of both phantoms. The microwave pulse is sent by the transmitting antenna to examine the health of the breast and throat, whereas the backscattering signals are collected by the receiving antenna that is reflected from both tissues. The experiment is performed two times for the breast phantom and three times for the throat model to examine the signal from tissues with and without tumors in order to find differences in signal levels.

Figure 16a shows the comparison between the measurement and simulation results of the S_{21} parameters of phantom with tumor and without tumor using VNA. It is noted that when the breast phantom with the presence of tumor further reflections than the breast phantom with the absence of tumor for both results. The simulated S_{21} results of the healthy throat are only compared with measured S_{21} results of a healthy man's throat due to not existing a throat with having tumor at this time. In addition, The simulated S_{21} results of the normal throat to the unhealthy throat with the first tumor and second tumor are given in Figure 16b. It is observed that the backscattering signals of the second tumor are more than the first tumor and the throat with no tumor and the reflected signal of the first tumor is greater than the normal throat. The reason for these results is due to variation between the dielectric properties of healthy tissue and those of tumor cells [26]. Subsequently, the S_{21} signals are converted to probability density function (PDF) using the equation (9) in MATLAB to see clearly the signal variations as given in Figure 16(c, d). variation in the S- parameter signal level causes the scattered field which is a significant issue for breast phantom scanners. Resulting in these variations, tumors or undesirable cells inside the human throat and breast can be detected and drawn.

$$f(x) = \frac{1}{\sigma\sqrt{2\pi}} e^{-\frac{1}{2}\left(\frac{x-\mu}{\sigma}\right)^2} \quad (9)$$

Where μ, σ are the mean and standard deviation respectively.

Power Loss Density (PLD) and Specific Absorption Rate (SAR) is evaluated without and without tumor for both tissues as shown in Figure 17 and 18. A uniform distribution of transmitted power over the normal tissues can be seen. A power pattern with a tumor shows a distribution of power that is not even and includes some power from the radiation absorbed by the tumor, which causes deflections and variation in power distribution. The density of the colors inside the breast with cancer is much higher than the density of the normal breast for the power loss density of 12652 W/m^3 as depicted in Figure 17(a,b). This difference in the color density results in having more different dielectric characteristics inside the phantom. Moreover, due to large sample tissues and reduced computational time, the specific absorption rate is studied for 0.01g at the frequency of 3 GHz . The maximum SAR for the normal and inflected breast by tumor is 21 W/kg , but the red color density in the unhealthy breast is higher than that

of the normal breast at the center of the phantom. Besides, the red color density inside the first and second tumors of the throat sample is high as compared with the normal tissue for the power loss density of 6000 w/m^3 . In addition, the specific absorption rate is studied for the throat section at the frequency of 3 GHz. The density of red color inside the first and second tumors of the throat model is higher than normal tissue at 3.3 W/kg as displayed in Figure 18(d,e,f) and the maximum SAR results in the first and second tumors is 16.75 and 16.89 W/kg respectively. In conclusion, the effects of tumors on the human body can be detected using the change between forward and reverse signals and the difference in color intensity of the power pattern.

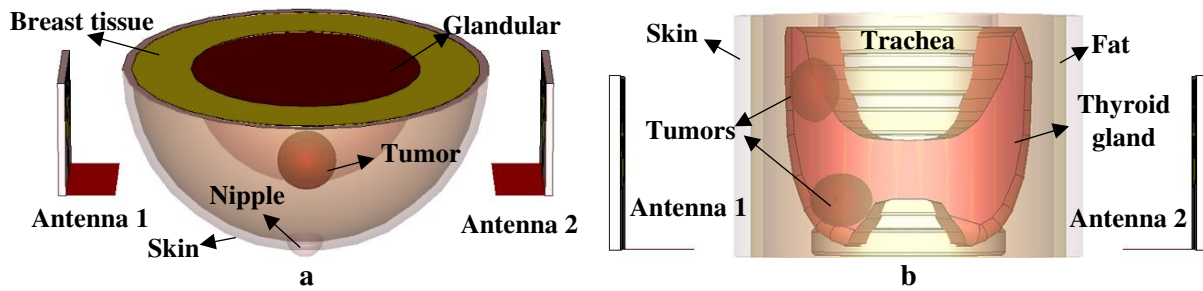


Fig. 15. Layout of (a) breast tissues and (b) throat model.

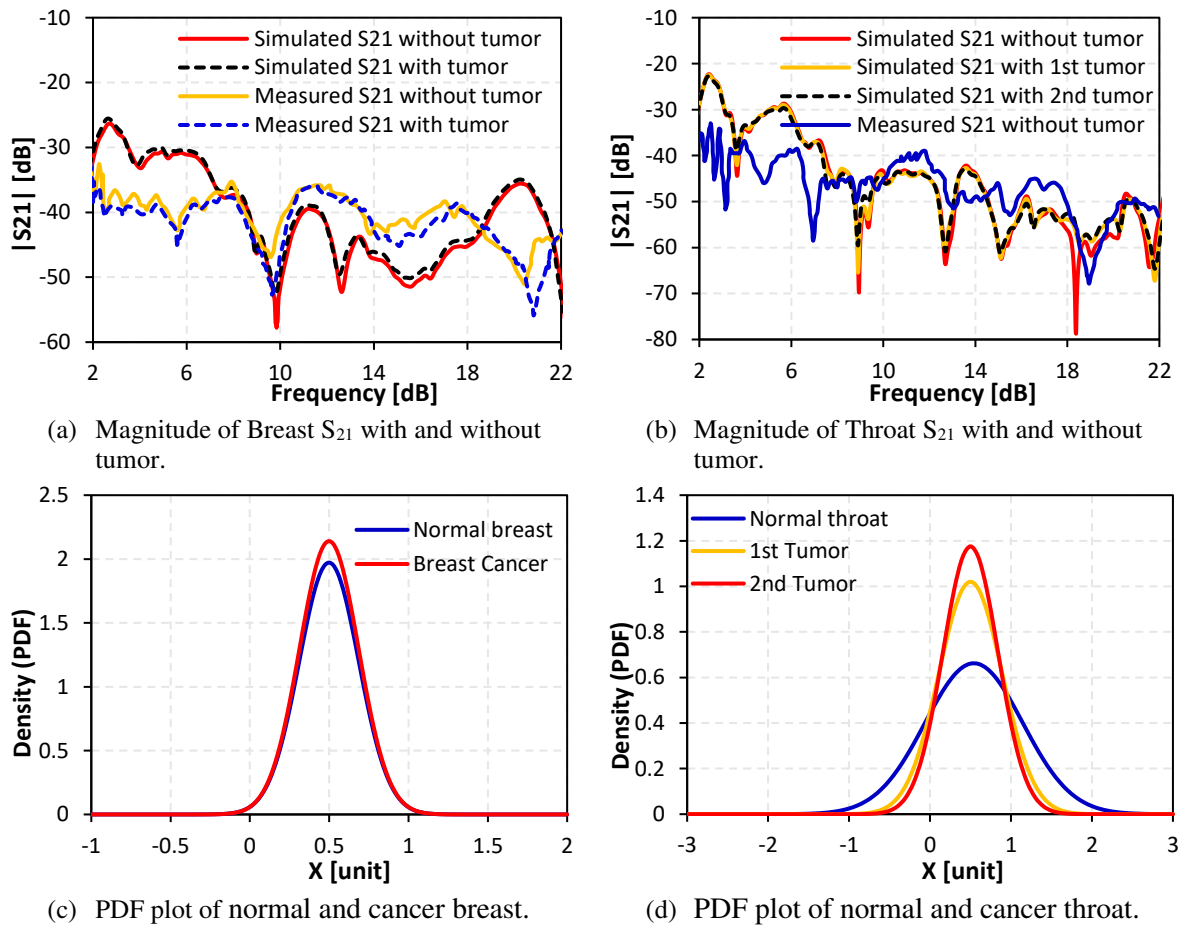


Fig. 16. S_{21} Magnitude and probability density function plot of normal and cancer tissue for breast and throat sample.

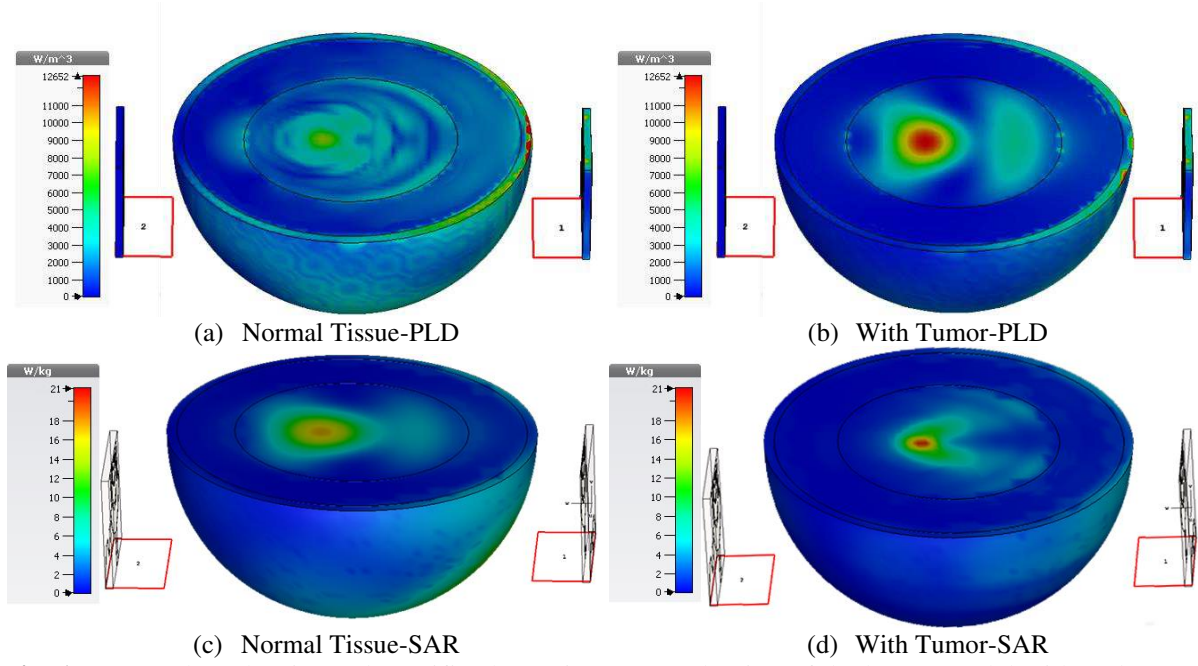


Fig. 17. Power loss density and specific absorption rate evaluation of the breast model with and without tumor.

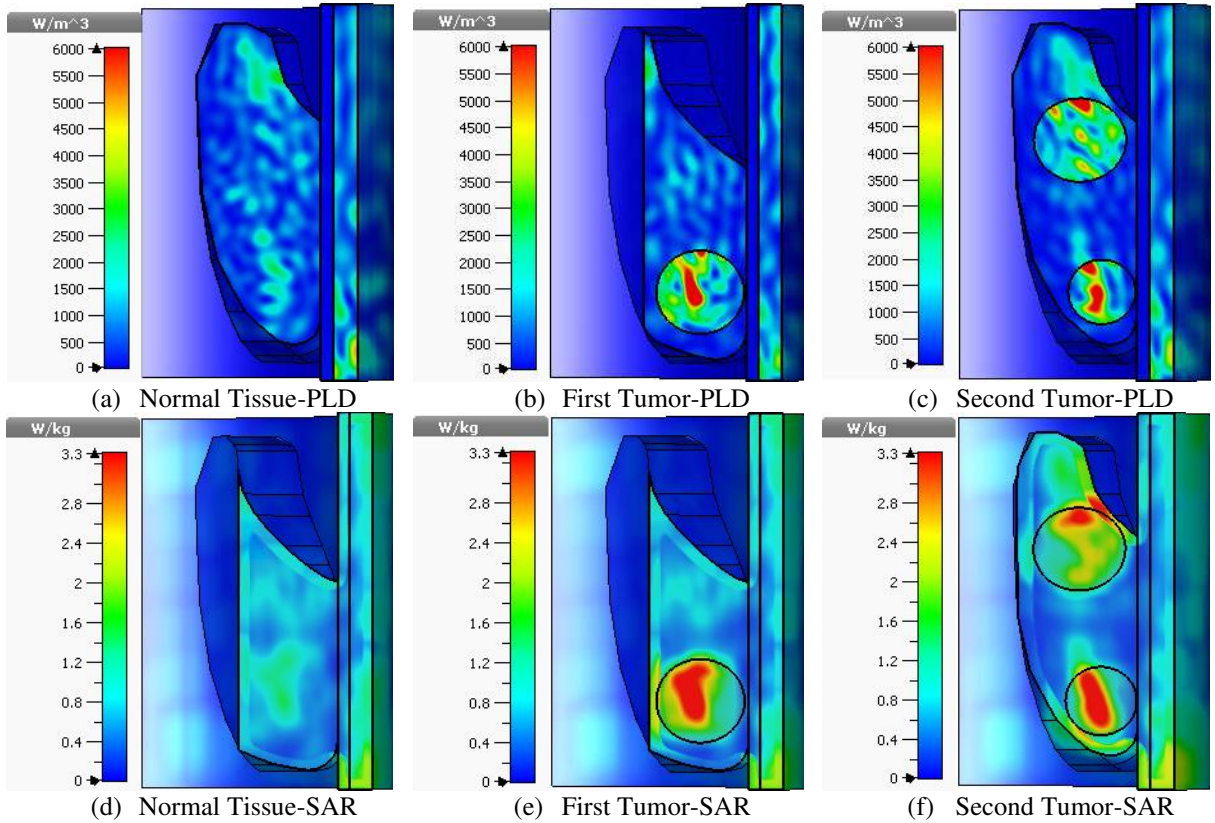


Fig. 18. Power loss density and specific absorption rate evaluation of the throat model with and without tumor.

The novel proposed UWB antenna is compared with other UWB planar antennas described in the literature for tumor detection as listed in Table 3. The comparison table shows that the overall size of the low-profile UWB antenna is smaller than those antennas described in recent references [22-31]. In addition, the fractural monopole antenna provides a low cost, a wide

operational frequency range, and a bigger bandwidth ratio (BWR) value compared with all references. The proposed antenna is used for analyzing breast tumor and throat tumors, whereas all various antennas in the table are designed for only the detection of tumor breast. Moreover, the proposed epsilon-UWB antenna provides a high magnitude realized gain as compared with the majority of antenna designs in Table 3.

Table 3. Comparison of the proposed UWB antenna with various listed antennas for tumor detection.

Ref.	Size [mm ²]	Frequency Range [GHz]	BWR:1	Substrate, h [mm], ϵ_r	Detection Tumor for	Gain
22	77.72 x 60	2.7–8.0	2.96	Rogers RT5880, 1.57 , 2.2	Breast	9.2 dBi
23	42 x 41	2.30–11.00	4.78	Rogers RT5880, 1.57 , 2.2	Breast	5.8 dBi
24	30 x 30	2-11	5.5	FR4, 1.6 , 4.4	Only simulated Breast	4.66 dBi
25	40 x 40	2.5-11	4.4	FR4, 1.6, 4.4	Breast	7.2 dBi
26	37 x 43	4.9-10.9	2.22	FR4, 1.57, 4.4	Breast using (petroleum jelly + wheat flour)	6.32 dB
27	77.72 x 60	2.7-11.2	4.15	Rogers RT5880, 1.57 , 2.2	Breast	-
28	80 x 61	2.42-3.3 4-15	1.36 3.75	Textile Materials, 6 , 1.44	Breast	7.56 dBi
30	40 x 40	3.01-11	3.65	FR4, 1.6, 4.4	Breast	7.1 dBi
31	76 x 78	3.1-7.6	2.45	FR4, 1.6, 4.6	Breast	6 dBi
Pro.	26 x 22	2.58-20.95	8.12	FR-4, 1.6, 4.4	Breast and throat	7.21 dB

8. Conclusion

This study presents a fractal antenna based on a novel epsilon-shaped geometry for UWB applications. A single ultra-wideband antenna is designed which operates in the frequency range from 2.58 GHz to around 21 GHz. The proposed low-profile antenna provides a low cost structure, a large bandwidth ratio of 8.12:1, a fractional bandwidth of 157%, and a well-realized gain of about 7.21 dB with the average achieved efficiency above 85% in the communication range. The novel antenna has a good ability to gather several wireless applications in this working range due to these appropriate antenna properties. This planar antenna is used in medicine to detect tumor cells in the breast and throat of humans. The measurement and simulation outcomes of the S_{21} parameters of the human body part with tumor and without tumor are compared using the CST software simulator and VNA. The Simulated and measured S_{21} parameters showed good agreement results in both cases. The power loss density, and specific absorption rate analysis indicated that the UWB antenna is suitable and safe for usage on the human body. Furthermore, the acceptable diversity metrics of the epsilon shape make this technology appropriate for wireless UWB, WiMAX, and any systems able to run in S, C, X, Ku, and K bands.

Acknowledgment

Erbil Polytechnic University and Urmia University assisted in the fabrication and support of the structures. As a result, the author wishes to express his gratitude to both universities for their contributions to this paper.

“Author Contributions: Conceptualization: Hiwa Sediq (H.S.); methodology: H.S., Javad Nourinia (J.N.) and Changiz Ghobadi (Ch.Gh.); software: H.S.; writing-original draft preparation: H.S.; writing-review and editing: J.N.; supervision: J.N., Ch.Gh., and H.S. All authors have read and agreed to the published version of the manuscript.

Funding: This research received no external funding.

Institutional Review Board Statement: Not applicable.

Informed Consent Statement: Not applicable.

Data Availability Statement: Not applicable.

Conflicts of Interest: The authors declare no conflict of interest.”

References

1. Sediq, H. T., Nourinia, J., Ghobadi, C., Alizadeh, F., Lalbakhsh, A., & Mohammadi, B. (2021, November). UWB Dual-notched Planar Antenna by Incorporating Single Compact EBG. In *2021 Photonics & Electromagnetics Research Symposium (PIERS)* (pp. 700-704). IEEE.
2. Jan, N. A., Kiani, S. H., Sehrai, D. A., Anjum, M. R., Iqbal, A., Abdullah, M., & Kim, S. (2021). Design of a compact monopole antenna for UWB applications. *CMC COMPUTERS MATERIALS & CONTINUA*, 66(1), 35-44.
3. Sediq, H. T. (2018). Design of ultra-wideband dipole antenna for WiMAX wireless applications. *Polytechnic Journal*, 8(3), 13-25.
4. Lakrit, S., Das, S., Ghosh, S., & Madhav, B. T. P. (2020). Compact UWB flexible elliptical CPW-fed antenna with triple notch bands for wireless communications. *International Journal of RF and Microwave Computer-Aided Engineering*, 30(7), e22201.
5. Rahman, M., Haider, A., & Naghshvarianjahromi, M. (2020). A systematic methodology for the time-domain ringing reduction in UWB band-notched antennas. *IEEE Antennas and Wireless Propagation Letters*, 19(3), 482-486.
6. Sediq, H. T., & Mohammed, Y. N. (2020). Performance analysis of novel multi-band monopole antenna for various broadband wireless applications. *Wireless Personal Communications*, 112(1), 571-585.
7. Okan, T. (2020). A compact octagonal-ring monopole antenna for super wideband applications. *Microwave and Optical Technology Letters*, 62(3), 1237-1244.
8. Sediq, H. T., Nourinia, J., Ghobadi, C., & Mohammadi, B. (2020). A Novel Eye-shaped Monopole Antenna for Wideband and 5G Applications. *IETE Journal of Research*, 1-11.
9. Alluri, S., & Rangaswamy, N. (2020). Compact high bandwidth dimension ratio steering-shaped super wideband antenna for future wireless communication applications. *Microwave and Optical Technology Letters*, 62(12), 3985-3991.
10. Cruz, J. D. N., Serres, A. J. R., De Oliveira, A. C., Xavier, G. V. R., De Albuquerque, C. C. R., Da Costa, E. G., & Freire, R. C. S. (2019). Bio-inspired printed monopole antenna applied to partial discharge detection. *Sensors*, 19(3), 628.
11. Zhang, S., Zhong, Y., Zhou, Y., Guo, Y., & Ji, C. (2019). Design of a symmetric open slot antenna for UWB applications. *IEICE Electronics Express*, 16-20190533.
12. Iqbal, A., Smida, A., Mallat, N. K., Islam, M. T., & Kim, S. (2019). A compact UWB antenna with independently controllable notch bands. *Sensors*, 19(6), 1411.
13. Ullah, S., Ruan, C., Sadiq, M. S., Haq, T. U., & He, W. (2020). High efficient and ultra wide band monopole antenna for microwave imaging and communication applications. *Sensors*, 20(1), 115.
14. Nakprasit, K., Sakonkanapong, A., & Phongcharoenpanich, C. (2020). Elliptical ring antenna excited by circular disc monopole for UWB communications. *International Journal of Antennas and Propagation*, 2020, 1-11.
15. Jan, N. A., Kiani, S. H., Sehrai, D. A., Anjum, M. R., Iqbal, A., Abdullah, M., & Kim, S. (2021). Design of a compact monopole antenna for UWB applications. *CMC- COMPUTERS MATERIALS & CONTINUA*, 66(1), 35-44.

16. Frank, M., Lurz, F., Kempf, M., Röber, J., Weigel, R., & Koelpin, A. (2020, January). Miniaturized ultra-wideband antenna design for human implants. In *IEEE Radio and Wireless Symposium (RWS)*, San Antonio, TX, USA, pp. 48-51.
17. Awan, W. A., Hussain, N., Naqvi, S. A., Iqbal, A., Striker, R., Mitra, D., & Braaten, B. D. (2020). A miniaturized wideband and multi-band on-demand reconfigurable antenna for compact and portable devices. *AEU-International Journal of Electronics and Communications*, 122, 153266.
18. Balani, W., Sarvagya, M., Samasgikar, A., Ali, T., & Kumar, P. (2021). Design and analysis of super wideband antenna for microwave applications. *Sensors*, 21(2), 477.
19. Kannappan, L., Palaniswamy, S. K., Kanagasabai, M., Kumar, P., Alsath, M., Kumar, S., & Pakkathillam, J. K. (2022). 3-D twelve-port multi-service diversity antenna for automotive communications. *Scientific reports*, 12(1), 1-22.
20. Koc Polat, H., Geyikoglu, M. D., & Cavusoglu, B. (2020). Modeling and validation of a new reconfigurable patch antenna through equivalent lumped circuit-based design for minimum tuning effort. *Microwave and Optical Technology Letters*, 62(6), 2335-2345.
21. M. Garcia and A. Jemal, "Global Cancer Facts and Figures 2011," Atlanta, GA: American Cancer Society, 2011.
22. Islam, M. T., Samsuzzaman, M., Kibria, S., Misran, N., & Islam, M. T. (2019). Metasurface loaded high gain antenna based microwave imaging using iteratively corrected delay multiply and sum algorithm. *Scientific reports*, 9(1), 1-14.
23. Hossain, A., Islam, M. T., Islam, M., Chowdhury, M. E., Rmili, H., & Samsuzzaman, M. (2020). A planar ultrawideband patch antenna array for microwave breast tumor detection. *Materials*, 13(21), 4918.
24. Rahayu, Y., Hilmi, M. F., & Masdar, H. (2019, July). A novel design rectangular UWB antenna array for microwave breast tumor detection. In *2019 16th International Conference on Quality in Research (QIR): International Symposium on Electrical and Computer Engineering* (pp. 1-5). IEEE.
25. Kibria, S., Samsuzzaman, M., Islam, M. T., Mahmud, M. Z., Misran, N., & Islam, M. T. (2019). Breast phantom imaging using iteratively corrected coherence factor delay and sum. *IEEE Access*, 7, 40822-40832.
26. Kaur, G., & Kaur, A. (2020). Breast tissue tumor detection using "S" parameter analysis with an UWB stacked aperture coupled microstrip patch antenna having a "+" shaped defected ground structure. *International Journal of Microwave and Wireless Technologies*, 12(7), 635-651.
27. Islam, M. T., Islam, M. T., Samsuzzaman, M., Kibria, S., & Chowdhury, M. E. (2021). Microwave Breast Imaging Using Compressed Sensing Approach of Iteratively Corrected Delay Multiply and Sum Beamforming. *Diagnostics*, 11(3), 470.
28. Hossain, K., Sabapathy, T., Jusoh, M., Lee, S. H., Rahman, K. S. A., & Kamarudin, M. R. (2022). Negative Index Metamaterial-Based Frequency-Reconfigurable Textile CPW Antenna for Microwave Imaging of Breast Cancer. *Sensors*, 22(4), 1626.
29. Furlow, P. W., & Mathisen, D. J. (2018). Surgical anatomy of the trachea. *Annals of cardiothoracic surgery*, 7(2), 255.
30. Islam, M. T., Samsuzzaman, M., Islam, M., Kibria, S., & Singh, M. J. (2018). A homogeneous breast phantom measurement system with an improved modified microwave imaging antenna sensor. *sensors*, 18(9), 2962.
31. Mahmud, M. Z., Islam, M. T., Misran, N., Kibria, S., & Samsuzzaman, M. (2018). Microwave imaging for breast tumor detection using uniplanar AMC based CPW-fed microstrip antenna. *IEEE Access*, 6, 44763-44775.